Numerical study of quasi-static and fatigue delamination growth in a post-buckled composite stiffened panel

A. Raimondo [*], S.A. Doesburg, C. Bisagni

Faculty of Aerospace Engineering, Delft University of Technology, Delft, The Netherlands

ARTICLE INFO

ABSTRACT

In this work, an approach based on the Virtual Crack Closure Technique, included in the commercial finite element code ABAQUS, is adopted to study the propagation of delamination in composite structures under quasi-static and fatigue loads. The methodology, originally capable of simulating only delamination under quasi-static loads, has recently been extended introducing the possibility to analyze damage progression under fatigue load condition. The approach is assessed on simple specimens, Double Cantilever Beam and Mixed Mode Bending test, comparing the results with literature data. Afterwards, the behavior of a single-stringer specimen with an initial delamination is numerically investigated considering compressive loading conditions. At first, the single-stringer specimen is analyzed under quasi-static compressive load showing a clear correlation between local buckling phenomena and delamination growth. Then, a cyclic compressive load is applied such that the specimen switches between pre- and post-buckling conditions in a single load cycle. The outcomes of the numerical analyses are compared with the experimental data obtained from an experimental test campaign previously performed, showing the advantages of the adopted numerical technique but also the limitations that need to be addressed to properly analyze this phenomenon.

1. Introduction

Modern thin-walled aeronautical structures, such as fuselage and wing structures, make extensive use of composite stiffened panels where the stringers are typically joined to the skin through adhesive bonding or co-curing. In most cases the buckling load of these structures is much lower than their failure load [1]. However, the out-of-plane displacements in the post-buckling regime may become considerably large, and, due to their cyclic occurrence, may induce separation in the interface between the skin and the stringer. The lack of reliable numerical procedures able to accurately predict this phenomenon forces to consider the buckling load as limit load during the design of aerospace stiffened panels. Allowing the structure to buckle in some well-defined service conditions would result in an increase of the load carrying capability or in a reduction of the structural weight at the same limit load. However, in this case, particular attention must be paid to fatigue delamination initiation and propagation to ensure that the panel does not fail prematurely.

Although the problem has been extensively studied at the coupon level, the prediction of fatigue delamination propagation in post-buckled stiffened composite panels is still an open issue. Under fatigue loading conditions, delamination growth is usually characterized using the power law proposed by Paris et al. [2,3], which relates the crack growth rate to the stress intensity factor or equivalently to the energy release rate. This law is widely accepted in literature and overall provides an excellent approximation of the experimental results. Nowadays almost all available numerical methodologies used to simulate fatigue delamination growth rely on the Paris law or on one of its variations. According to how the delamination is numerically represented and how the Paris law is implemented, the numerical approaches can be divided in two main categories, namely, damage mechanics and fracture mechanics [4].

In the context of damage mechanics, interface elements with an embedded cohesive law have been widely adopted for the simulation of delamination onset and propagation under quasi-static and impact load conditions [5–8]. Following the good results obtained for these problems, a few authors have extended cohesive formulation to simulate fatigue crack growth. However, inside the cohesive law, the energy release rate is not directly defined and this has led to the development of a variety of models that relate the cohesive damage variable to the crack

growth rate defined by the Paris law [9–12]. The majority of these models provide good results in analyzing fatigue crack propagation in small coupons. However, it is difficult to apply them to more complex structural problems due to the large number of interface elements required to adequately represent the fatigue cohesive zone resulting in unfeasible computational times.

On the other hand, numerical approaches derived from the fracture mechanics are based on the direct application of the Paris law in conjunction with a methodology for the calculation of the energy release rate, such as the Virtual Crack Closure Technique (VCCT) [13–15]. This approach, developed for simulating delamination propagation under quasi-static load conditions [16], is now implemented into several commercial Finite Element (FE) codes. A number of issues with the original VCCT formulation, such as the problem of orthogonality between the crack front and the structural mesh or the bi-material interface simulation, have been identified and addressed by a variety of researchers across a large number of publications [17–19].

Although this methodology has still some limitations when dealing with fatigue delamination problems [20] and requires an initial damage, it currently represents an effective solution for the simulation of fatigue crack growth in structural components.

The aim of this work is to study the delamination growth behavior in a composite single-stringer specimen with an initial delamination, subjected to cyclic load in post-buckling regime, using a VCCT based approach recently introduced in the FE Code ABAQUS [21]. The Single-Stringer Compression (SSC) specimen analyzed in this work has been designed and tested in Refs. [22–26] to be representative of the response of large multi-stringer panels such as those of aircraft fuselage structures. In the building block approach, commonly used for aerospace composite structures, the specimen fits between the coupon specimen level and the large multi-stringer stiffened panel level. The SSC specimen has been designed to have a small size and a relatively low manufacturing cost, while having a structural complexity on the level of multi-stringer panels. The intent is to improve the ease and affordability with which the response of stiffened panels can be experimentally determined, enabling the study of their failure behavior and damage tolerance in the post-buckling regime. This specimen provides the opportunity to verify and validate quasi-static and fatigue damage models due to its relatively complex geometry compared to coupon specimens, and its small size, which makes it computationally tractable.

In section 2 the theoretical background of the adopted numerical formulation is illustrated, while, in section 3, simple specimens such as the Double Cantilevered Beam (DCB) and the Mixed Mode Bending (MMB) test specimens are numerically analyzed to verify the effectiveness of the approach. Finally, in section 4, the model of the SSC specimen is presented together with the results of the quasi-static and fatigue numerical analyses and is compared with experimental data.

2. Theoretical background

The Paris Law used to characterize the fatigue crack growth rate is given, in its most basic form, in equation (1):

$$\frac{da}{dN} = C f(G)^m \tag{1}$$

where C and m are fitting parameters and $f(G)$ is a function of the energy release rate (G). The typical behavior of the crack growth rate is qualitatively shown in Fig. 1.

The curve in Fig. 1 can be divided into three distinct regions. In region I, a sharp drop in the crack growth rate occurs when the energy release rate approaches the threshold value (G_{th}), which depends on the material and on the loading conditions. In region II the behavior is almost log-linear and is captured by the Paris law. In region III, when the energy release rate approaches the critical value (G_c), the crack growth rate drastically increases.
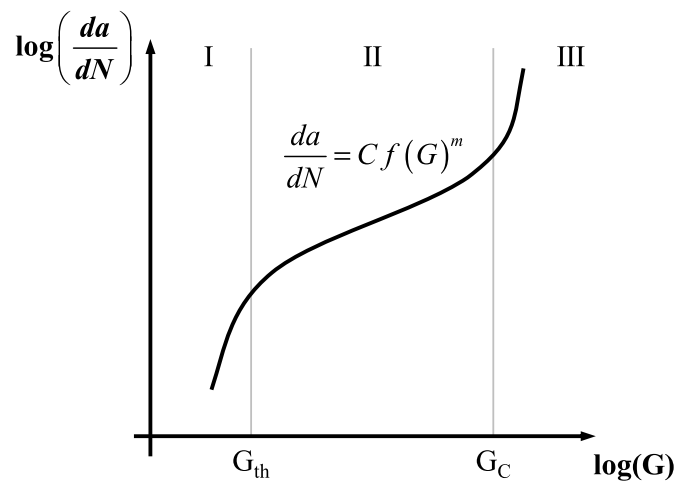

Fig. 1. Typical fatigue crack growth curve.

Many different functions of G can be found in literature [4,27] and there is no clear consensus on which function better describes the experimental data. Most of the formulations tend to adopt G_{max}, or $\Delta G = G_{max}\text{-}G_{min}$, respectively, the maximum value of the energy release rate and the variation of the energy release rate during the load cycle. However, as pointed out by Pascoe et al. in Ref. [27], since the delamination growth is ultimately driven by the applied fatigue cycle, which cannot be described by a single parameter, any equation which use only one parameter is not able to fully capture the delamination growth behavior. Furthermore, the use of ΔG can result in an erroneous interpretation of experimental data since it violates the principle of similitude. Based on the analogy with the stress intensity factor variation (ΔK), adopted for fatigue crack growth in metal, according to Ref. [27], the parameter $((G_{max})^{0.5}\text{-}(G_{min})^{0.5})^2$ seems to provide a better description of experimental results.

Despite these limitations, the large majority of experimental data available in literature are reported using the variation of the energy release rate during each load cycle, as shown in equation (2):

$$\frac{da}{dN} = C(\Delta G)^m = C(G_{max} - G_{min})^m \tag{2}$$

The methodology adopted in this work and included in the FE code ABAQUS [21] is based on equation (2) for the calculation of the crack growth rate and on the VCCT equations to evaluate the energy release rate.

The VCCT is based on Irwin's assumption [28] that the strain energy released when a crack extends by a small amount Δa from a to $a+\Delta a$ is equal to the work required to close the crack to its original length, a. In the framework of a finite element analysis, assuming that the extension Δa does not change significantly the state of stress along the crack front, it is possible to evaluate the energy release rate considering the forces acting on the node at the delamination front and the displacements of the nodes immediately behind it, as shown in Fig. 2 for a 2D problem.

The mode I and mode II components of the energy release rate can be calculated, referring to Fig. 2, using Equation (3):

$$G_I = \frac{1}{2\Delta a} Z_1 \Delta w_{2,3} \qquad G_{II} = \frac{1}{2\Delta a} X_1 \Delta u_{2,3} \tag{3}$$

where X_1 and Z_1 are the shear and opening forces at crack tip (node 1), $\Delta u_{2,3}$ and $\Delta w_{2,3}$ are the relative shear and opening displacements at upper and lower crack face in the nodes behind the crack tip (node 2 and 3) and Δa is the increment in the crack length.

The propagation condition in a quasi-static analysis is reached when the sum of all the components of the energy release rate reaches the fracture toughness of the material. Several criteria exist for the calculation of the fracture toughness in a general 3D case involving all the
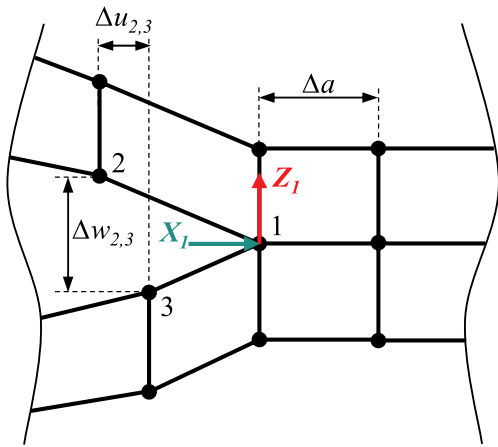
Fig. 2. Virtual crack closure technique.

three opening modes. One of the most adopted methods is the Benzeggagh-Kenane criterion [29], shown in equation (4):

$$G_c = G_{Ic} + (G_{IIc} - G_{Ic})\left(\frac{G_{II} + G_{III}}{G_I + G_{II} + G_{III}}\right)^{\eta} \qquad (4)$$

where G_{Ic} and G_{IIc} are the fracture toughness for pure mode I and mode II, while η is a fitting parameter obtained from experimental data. The propagation criterion adopted in ABAQUS can be expressed as follow:

$$1 \le \frac{G}{G_c} \le 1 + f_{tol} \qquad (5)$$

where f_{tol} is the release tolerance, whose default value is 0.2. It is possible to reduce this value to improve the accuracy of the analysis but this results in an increase in the computational times.

Once the propagation criterion is met, by default, the connection between the two coincident nodes on the delamination front is instantaneously released. It is also possible to define a ramp behavior in which the constrained force is linearly reduced to zero with the opening displacement, according to the value of the fracture toughness. This non-default approach allows to improve the convergence ratio of the analysis and to better capture rounded delamination fronts. However, ramp debonding is not currently supported for fatigue analyses where only the instantaneous release is available.

The fatigue crack growth analysis capability in ABAQUS adopts the same VCCT equations to evaluate the energy release rate. The procedure requires to define the load history of a single load cycle. Because only constant amplitude fatigue loads can be simulated, the load cycle remains the same up to the total number of cycles specified by the user. The solution of each load cycle is obtained using the static nonlinear algorithm of the ABAQUS/Standard solver. The values of G_{min} and G_{max}, and therefore ΔG, are calculated using the VCCT equations when the structure is subjected respectively to the minimum and maximum load during the load cycle. The onset of fatigue delamination growth is determined with a criterion based on both G_{max} and ΔG. The first part of the criterion consists in an exponential curve fit of the experimental fatigue crack onset data for the material being tested. In addition, the value of G_{max} must exceed the threshold energy release rate of the material (G_{th}). The conditions that must be met for delamination to begin propagating are summarized in equation (6):

$$f = \frac{N}{c_1 \Delta G^{c_2}} \ge 1 \wedge G_{max} > G_{th} \qquad (6)$$

where N is the current cycle number and c_1 and c_2 are fitting parameters experimentally determined. Once the onset criteria are satisfied, the fatigue delamination growth rate is governed by the Paris law shown in equation (7).

$$\frac{da}{dN} = c_3 (\Delta G)^{c_4} \qquad (7)$$

where c_3 and c_4 are fitting parameters.

The algorithm adopts a damage extrapolation technique to avoid the simulation of the entire load history. In particular, if at the end of the load cycle N, the onset criteria are satisfied in at least one point along the delamination front, the crack length is extended from the actual value a_N to $a_{N+\Delta N}$ by releasing one node. The number of cycles required for the crack to grow is evaluated at each node along the crack tip reversing the Paris law, as shown in equation (8):

$$\Delta N_j = \frac{\Delta a_{N_j}}{c_3 \Delta G^{c_4}} \qquad (8)$$

where ΔN_j is the number of cycles required to release the node J, and Δa_{Nj} is the crack extension that produces the release of the node J. The procedure releases at least one node at each load cycle by choosing the node with the minimum value of the cycles number evaluated with equation (8). This value also represents the number of cycles that are jumped in the following increment. The procedure is schematically illustrated in Fig. 3.

It is possible to accelerate this process defining a non-zero tolerance ΔD_{Ntol} which allows to release in the same cycle more than one node as long as the relation expressed in equation (9) is satisfied:

$$\frac{Log\Delta N_j - Log\Delta N_{min}}{Log\Delta N_{min}} \le \Delta D_{Ntol} \qquad (9)$$

The damage extrapolation tolerance determines how many nodes are released at each load cycle taking into account how close, in terms of number of cycles at failure (ΔN_j), any other node on the delamination front is with respect to the weakest node (ΔN_{min}). A less stringent tolerance reduces the computational time, since more nodes can be released in a single load cycle, however the accuracy of the analysis decreases. The default value of ΔD_{Ntol} is 0.1.

3. Numerical analysis of coupon tests

The numerical procedure described in the previous section is adopted at first to analyze two test cases, the Double Cantilevered Beam (DCB) and the Mixed Mode Bending (MMB) specimens, so to investigate the response of the numerical algorithm for crack propagation under pure mode I and mixed-mode condition. The specimens are investigated through quasi-static delamination propagation analyses and then using the fatigue crack propagation algorithm. The results of the numerical analyses are compared with benchmark data taken from literature [30–32].

3.1. Analysis of DCB test

The DCB specimen is a widely recognized standard to determine the mode I inter-laminar fracture toughness [33] and mode I fatigue crack
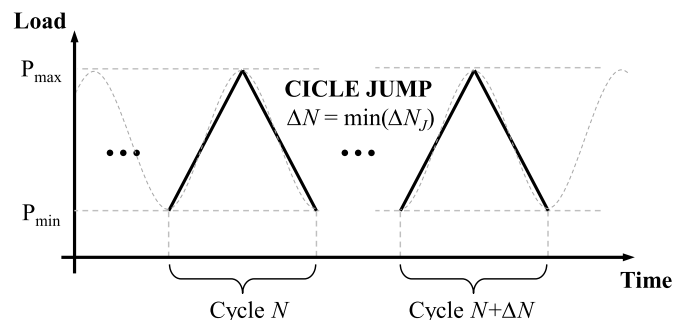

Fig. 3. Schematic representation of fatigue crack growth analysis.

growth [34] for unidirectional fiber composite materials. The geometrical characteristics of the DCB specimen analyzed in this study are taken from literature [30] and shown in Fig. 4.

The specimen is made of T300/1076 graphite/epoxy with 24 unidirectional plies and an initial delamination positioned in the center of the thickness. The properties of the material adopted in the numerical analyses are taken from literature [30] and shown in Table 1.

The FE model is realized using continuum shell elements (SC8R) with element length of 0.5 mm in the propagation area and 1 mm in the remaining part of the specimen. One element is used through the thickness of each arm. The mesh density was chosen through a preliminary convergence study performed using two models with an element length in the propagation area of respectively 0.5 and 1.3 mm. Although the results of the model with a coarse discretization were already sufficiently accurate, the use of an element length of 0.5 mm further improves the results without resulting in a significant increase in the computational time. The two arms are modeled to have coincident nodes at the interface to increase the convergence ratio of the numerical analysis. A value of 0.1 is adopted for the release tolerance of the VCCT algorithm. The nodes belonging to the end edge of the specimen are constrained, while an opening displacement is applied to the nodes of the delaminated end. The FE model with the applied boundary conditions is shown in Fig. 5.

The load-displacement curve of the quasi-static analysis performed on the DCB model is presented in Fig. 6, along with the benchmark results from Krueger [30].

The model shows a linear response until the delamination begins to propagate at the peak reaction force. There is a good agreement between the numerical results and the reference data, both in terms of initial stiffness and peak load, which differs from the benchmark by less than 2%. In Fig. 7 the deformed shape of the structure is shown together with the bonded status of the nodes at the interface at different values of the applied opening displacement.

The delamination during the propagation shows a slightly rounded crack front, as expected from comparison with literature experimental results [30].

The same DCB specimen is then analyzed under fatigue loading conditions using the parameters shown in Table 2, taken from literature [31].

The coefficients r_1 and r_2 in Table 2 represent the lower and upper fatigue growth thresholds, and can be defined respectively as:

$$r_1 = \frac{G_{th}}{G_c} \qquad r_2 = \frac{G_{pl}}{G_c} \qquad (10)$$

where G_{pl} is the Paris limit energy release rate when the crack growth rate reaches the unstable growth region. If the energy release rate is below G_{th} no delamination growth is assumed to occur, while, if it is above G_{pl}, quasi-static delamination growth is assumed to occur and the fatigue delamination growth analysis is terminated. The default value of 0.1 is adopted for the fatigue release tolerance ΔD_{Ntol}.

The analysis is divided into two steps: a pre-load step, where the opening displacement is increased up to the minimum displacement of
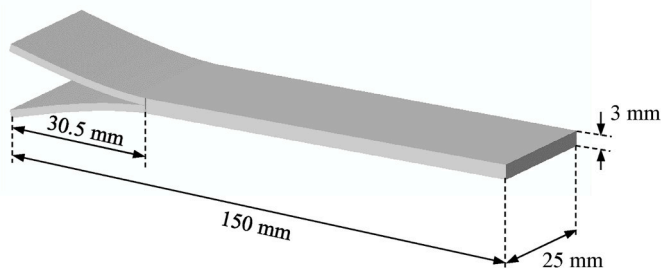
Table 1
Material properties of T300/1076.

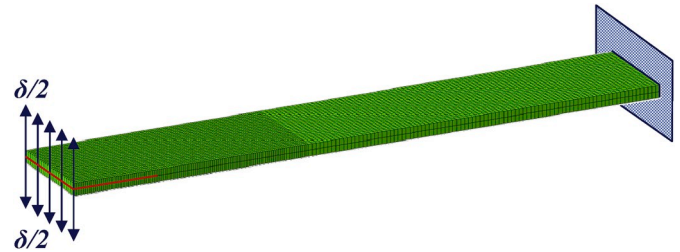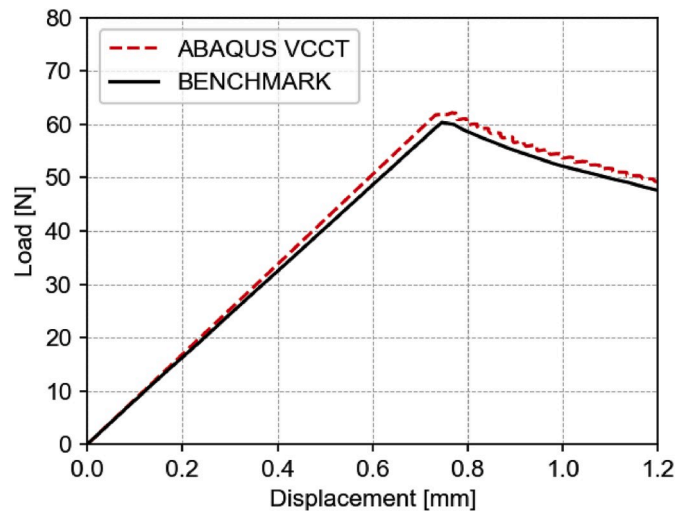| Property	Unit	Value
E_1	[MPa]	139400
$E_2 = E_3$	[MPa]	10160
$G_{12} = G_{13}$	[MPa]	4600
G_{23}	[MPa]	3540
$\nu_{12} = \nu_{13}$		0.30
ν_{23}		0.436
G_{1C}	[kJ/m^2]	0.17
G_{2C}	[kJ/m^2]	0.49
η		1.62

Fig. 5. DCB FE model.

Fig. 6. Load-displacement curves of DCB specimen from quasi-static analysis.

the fatigue cycle δ_{min}, and the fatigue step, where the displacement oscillates from the minimum to the maximum displacement δ_{max} of the load cycle. A triangular load cycle is defined starting from the minimum applied displacement at step time 0, rising linearly to the maximum applied displacement at step time 0.5 and decreasing linearly back to the minimum applied displacement at step time 1. The load steps are schematically illustrated in Fig. 8.

The delamination length measured at the center of the specimen as function of the number of cycles is shown in Fig. 9 comparing it with benchmark results taken from literature [31].

As expected with a displacement controlled analysis, the delamination length rapidly increases in the first load cycles, then the growth rate decreases until the energy release rate becomes smaller than the growth threshold and the delamination stops propagating around 3.7 million cycles. From Fig. 9, the agreement between the numerical results and the benchmark data can be appreciated, with the two curves deviating by less than 1%. The delamination front at different cycles is shown in Fig. 10.

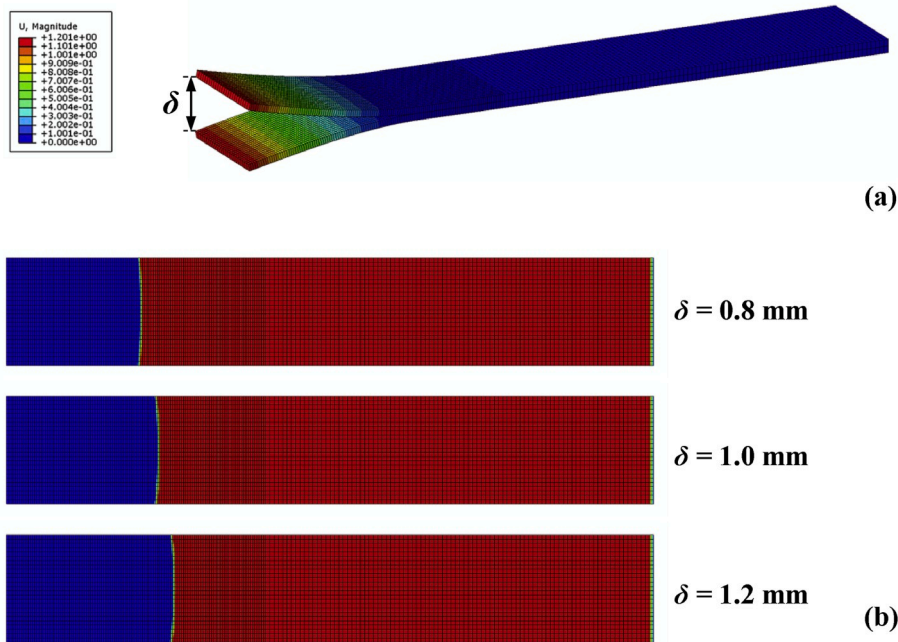It can be noticed, from Fig. 10, that the delamination starts in the

Fig. 4. DCB specimen geometry.

(a)

$\delta = 0.8$ mm

$\delta = 1.0$ mm

$\delta = 1.2$ mm

(b)

Fig. 7. Quasi-static analysis of DCB specimen: (a) deformed shape; (b) delamination front.

Table 2
Fatigue parameters of T300/1076.

Fatigue parameters		
$\delta_{max}/2$	[mm]	0.67
$\delta_{min}/2$	[mm]	0.067
R		0.1
c1		2.8461E-9
c2		−12.415
c3		2.44E6
c4		10.61
r1		0.353
r2		0.9
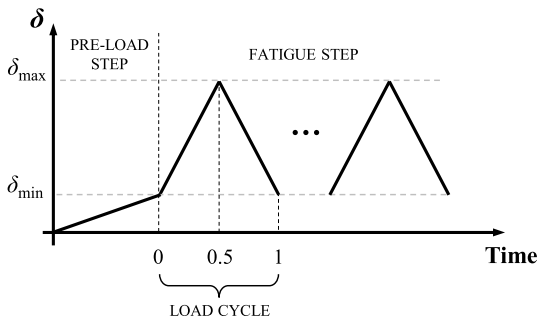
Fig. 8. Schematically representation of fatigue load steps.

center of the specimen and grows with the same rounded crack front observed in the quasi-static analysis, although the absence of the ramp release option in the fatigue analysis results in a much less smooth delamination front compared to the one of the static analysis shown in Fig. 7.

3.2. Analysis of MMB test

The MMB specimen is one of the standard specimens to determine mixed-mode crack propagation for static and fatigue loading conditions [35]. The geometrical characteristics of the specimen and of the load
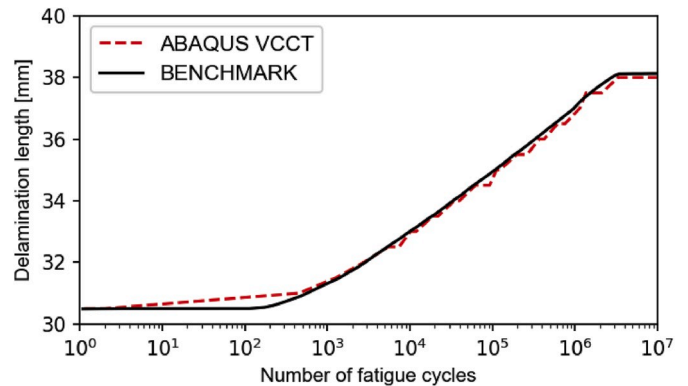

Fig. 9. Fatigue delamination propagation in DCB specimen.

448 Cycles

10,214 Cycles

37,013 Cycles

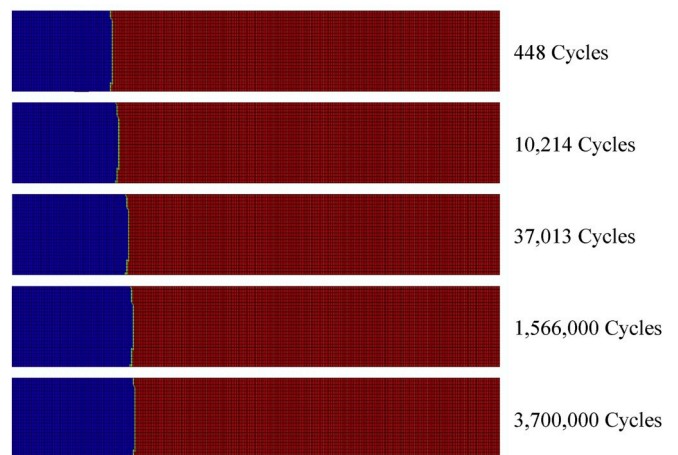1,566,000 Cycles

3,700,000 Cycles

Fig. 10. Delamination front at different load cycles in DCB specimen.

fixture, considered in this study are taken from literature [32], and are shown in Fig. 11.

The specimen has 24 unidirectional plies of carbon epoxy IM7/8552 with a delamination in the middle of the thickness. The material properties are taken from literature [32] and are reported in Table 3.

The mode-mixity at the delamination front of the MMB specimen depends on the length of the lever, *c*. Two different values of the lever length, which produce a mode-mixity of 50% and 80%, are analyzed in this work and reported in Table 4.

The same mesh discretization adopted for the DCB is used to model the MMB specimen. Two layers of continuum shell elements (SC8R) with coincident nodes are employed to model the arms of the specimen, while discrete rigid elements (R3D4) are selected to represent the load fixture.

The bottom part of the fixture is encased, a tie constraint is used to pin the loaded edge of the specimen to the fixture, while a surface-to-surface contact condition is defined between the other edge of the bottom fixture and the bottom surface of the specimen to allow sliding and avoid interpenetrations. Similarly, the top fixture is pinned to the loaded edge of the specimen and a surface-to-surface contact interaction between the sliding edge of the fixture and the top surface of the specimen is defined. The FE model and the boundary conditions are illustrated in Fig. 12.

Since no relevant differences exist between the MMB models at different mode-mixities, only the results of the 50% mode-mixity are presented for the quasi-static delamination propagation analysis. A value of 0.1 is adopted for the release tolerance of the VCCT algorithm. The results in terms of load versus applied displacement are shown in Fig. 13 compared with benchmark data taken from literature [32].

A linear response is observed until the delamination propagation occurs and the reaction force decreases. When the crack front reaches the lever contact point at half span of the specimen, the change in the contact conditions leads to an increase in the reaction force. The stiffness of the model as well as the behavior after the propagation agree well with the benchmark results. The deformed shape of the specimen and the delamination front at the end of the analysis are presented in Fig. 14.

In Fig. 14 it can be noted, as already seen for the DCB, that the numerical analysis predicts the delamination front shape observed in experimental tests [32].

To analyze the specimen under fatigue loading conditions the parameters shown in Table 5, taken from literature [32], are adopted. The maximum displacements were determined to produce a maximum value of the energy release rate at the delamination front equal to 60% of G_c. A release tolerance ΔD_{Ntol} of 0.001 is adopted for the fatigue analysis.

The results of the numerical analysis in terms of delamination length versus the number of cycles are reported and compared with the benchmark data in Fig. 15.

Also in this case, there is a good match between the numerical results and the benchmark data, although a quite large deviation can be observed at the end of the analysis. In both cases, the differences begin to occur when the crack length reaches the mid-span length of the specimen, suggesting that a more accurate modeling of the load fixture including friction effects may be needed.
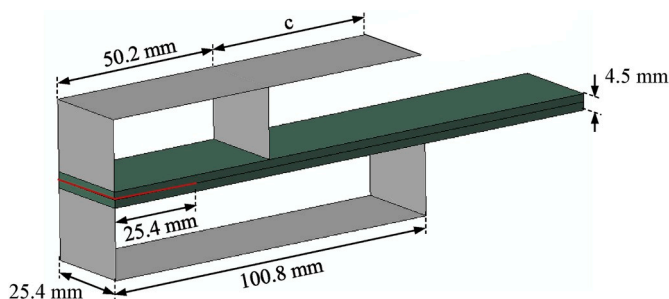
Table 3
Material properties of IM7/8552.

Property	Unit	Value
E_1	[MPa]	161000
$E_2 = E_3$	[MPa]	11380
$G_{12} = G_{13}$	[MPa]	5200
G_{23}	[MPa]	3900
$\nu_{12} = \nu_{13}$		0.32
ν_{23}		0.45
G_{1C}	[kJ/m^2]	0.212
G_{2C}	[kJ/m^2]	0.774
η		2.1

Table 4
Length of lever at different mode-mixity.

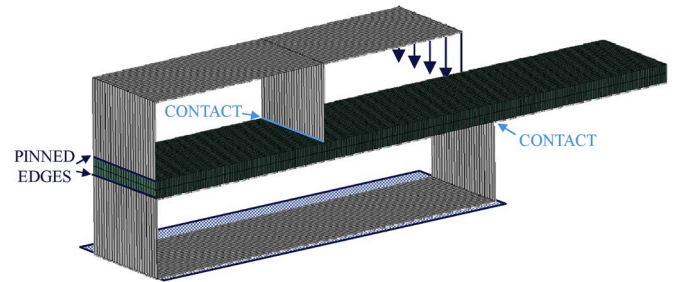| Lever length		
$C_{50\%}$	[mm]	41.3
$C_{80\%}$	[mm]	27.3

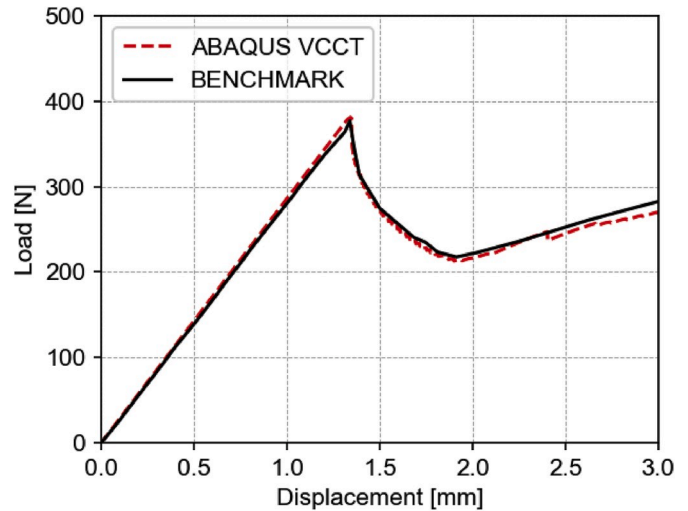**Fig. 12.** MMB FE model.

Fig. 13. Load-displacement curves of 50% MMB specimen from quasi-static analysis.

4. Single-stringer compression specimen

In this section, the quasi-static and fatigue response of the SSC specimen, developed and tested in Refs. [22–26], is numerically investigated. The specimen consists of an omega-shaped stringer co-cured with a skin panel. An initial delamination of 40 mm is created under one of the stringer flanges in the middle of the specimen, using a Teflon insert during the manufacturing process. The geometrical characteristics of the stiffened panel are shown in Fig. 16.
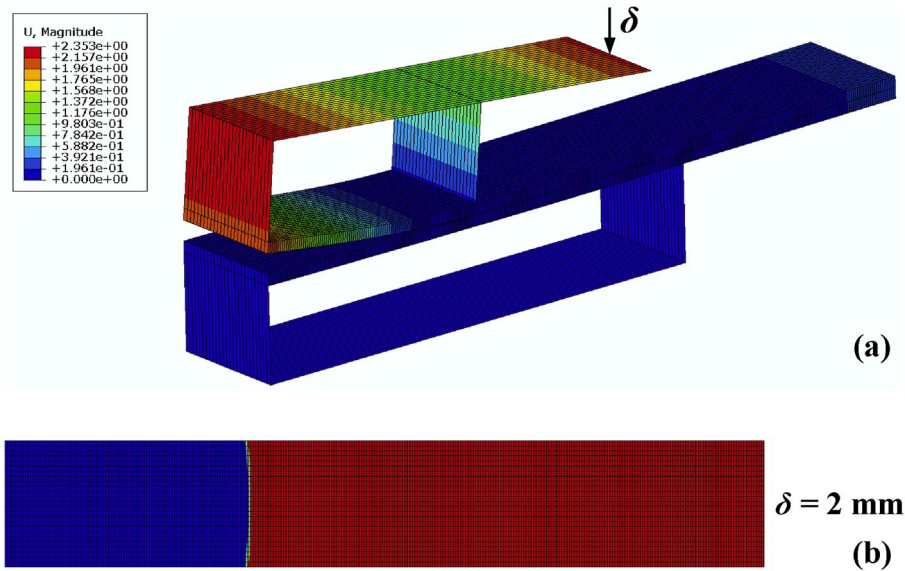
Fig. 11. MMB test geometry.

Fig. 14. Quasi-static analysis of 50% MMB specimen: (a) deformed shape; (b) delamination front.

Table 5
Fatigue parameters of IM7/8552.

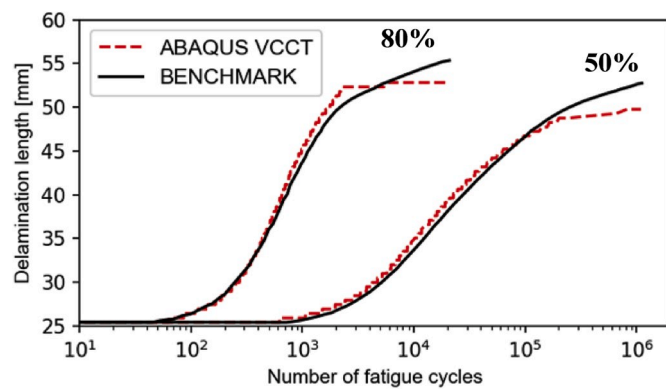| Fatigue parameters					
50% Mixed-Mode			80% Mixed-Mode		
δ_{max}	[mm]	1.04	δ_{max}	[mm]	1.28
δ_{min}	[mm]	0.104	δ_{min}	[mm]	0.128
R		0.1	R		0.1
c1		9E-5	c1		5.6E-3
c2		−9.71	c2		−8.0
c3		6.79	c3		4.5788
c4		5.4	c4		5.1
r1		0.186	r1		0.11
r2		0.9	r2		0.9

Fig. 15. Fatigue delamination propagation in MMB specimen.

The skin is made of 8 unidirectional plies of carbon-epoxy IM7/8552 with a quasi-isotropic layup [45/90/-45/0]s, while 7 plies with layup [-45/0/45/0/45/0/-45] are used for the stringer. Although the material system is the same as the MMB specimen analyzed in the previous section, the properties reported in Ref. [32] are slightly different from those shown in Table 4 due to two different versions of the same material distributed in Europe and in the United States. The material properties from Ref. [25], reported in Table 6, are adopted in this numerical simulation.

The model is discretized using a 1 mm uniform mesh of continuum shell elements (SC8R). The two flanges of the stringer are connected to the skin in the undamaged region defining the VCCT contact interaction to simulate the propagation of the delamination, while in the delaminated area a surface-to-surface contact interaction is introduced to prevent interpenetration between the skin and the stringer flange. Two reference points are defined on the opposite ends of the specimen, and the nodes on the edges are constrained to their respective reference point with rigid body ties. One reference point is encased, while for the reference point on the opposite end all degrees of freedom except the displacement along the longitudinal axis of the specimen are constrained.

The potting of the specimen is simulated restraining the displacements of the nodes in the potted regions but leaving them free to move along the longitudinal axis. The FE model and the boundary conditions are shown in Fig. 17.

To facilitate the transition through the buckling bifurcation point and avoid convergence issues during the application of the compressive load, a small initial geometrical imperfection is applied to the model. The nodal coordinates are modified adding 1% of the displacements extracted from the first buckling mode shape obtained from an eigenvalue analysis. This shape corresponds to the buckling mode observed in experimental tests, and consists of three half-waves as shown in Fig. 18.

The quasi-static delamination propagation analysis is conducted under displacement control, imposing a compressive displacement to the reference point unrestricted in the axial direction. The release tolerance of the VCCT algorithm is increased to 0.3 to reduce the computational load. A preliminary analysis using a tolerance of 0.1 has not shown any significant improvement while resulting in an increase in the computational time. Fig. 19 shows the obtained load-displacement curve and compares it to the experimental data measured during two quasi-static tests [24].

The initial trend of the obtained load-displacement curve reported in Fig. 19 matches the experimental curves, although a difference in stiffness between the numerical results and the experimental data can be observed. This may be due to one or a combination of different types of imperfections. The test specimens contain geometrical imperfections such as variation in the potting length, alignment of the loaded surfaces of the potting, alignment of the specimen to the loaded surfaces and flatness of the specimen. In addition to these imperfections part of the difference may also be caused by the assumed boundary conditions to model the potting. Furthermore, from Fig. 19 it is possible to notice that the numerical model quite underestimates the first load drop and
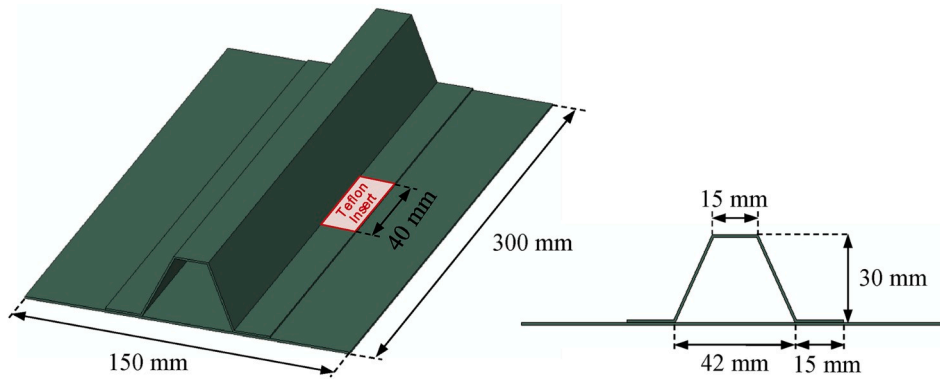
Fig. 16. SSC specimen geometry.

Table 6
Material properties of IM7/8552 for SSC specimen analysis.

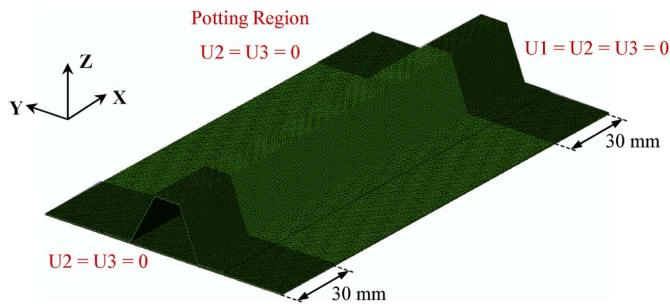| Property	Unit	Value
E_1	[MPa]	150000
$E_2 = E_3$	[MPa]	9080
$G_{12} = G_{13}$	[MPa]	5290
G_{23}	[MPa]	3400
$\nu_{12} = \nu_{13}$		0.32
ν_{23}		0.45
G_{1C}	[kJ/m^2]	0.277
G_{2C}	[kJ/m^2]	0.788
η		1.63

Fig. 17. SSC specimen FE model.
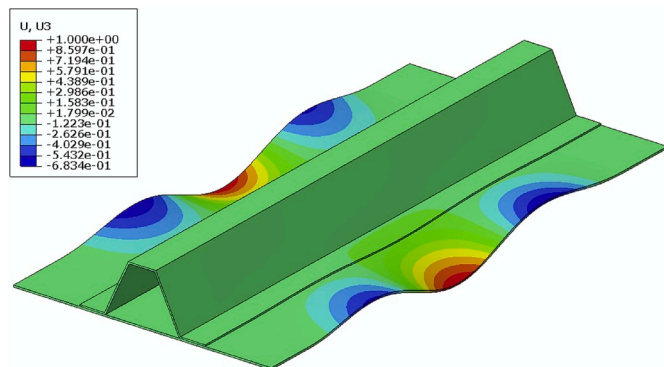
Fig. 18. First eigenmode of SSC specimen (displacements amplified by a factor of 10).

Fig. 19. Load-displacement curves of SSC specimen from quasi-static analysis.

performing experimental tests according to the ASTM standards [33–35] on coupons with delamination positioned between 0° plies. In the specimen under investigation, the initial delamination is located in the 45°/-45° interface resulting in higher values of the fracture toughness and higher delamination growth resistance. Indeed, further experimental tests are needed to correctly measure the value of the fracture toughness at the interface considering the orientation of the plies of the specimen.

The specimen starts to buckle at an applied displacement of around 0.13 mm with a reaction force of 7.1 kN, then the increase of the out-of-plane displacements causes the opening of the delamination. The energy release rate reaches the critical value in several locations along the crack front at an applied displacement of 0.27 mm and a reaction force of 13.8 kN, initiating the propagation of the delamination.

Observing the graph in Fig. 19, three load drops can be seen at 0.37 mm, 0.49 mm and 0.62 mm. These sudden losses of stiffness correlate with shifts in the buckling mode shape of the delaminated stringer flange section as shown in Fig. 20, where the deformed shapes of the model with out-of-plane displacements contour plot are presented together with the delamination front at different values of the applied displacement.

Initially the skin buckles in three half-waves (Fig. 20a), which corresponds to the shape of the applied initial imperfections. The first, and largest, load drop occurs when the delaminated section of the stringer flange buckles locally into a single half-wave shape, the skin on the delamination side shifts to a single half-wave shape, while, on the other side, the mode shape inverts its direction (Fig. 20b). The second load drop correlates with the locally buckled section of the stringer flange jumping from single half-wave to a two half-waves shape (Fig. 20c) and then changing again to three half-waves (Fig. 20d). Up to 0.37 mm the delamination propagates equally on both sides, while after 0.37 mm it
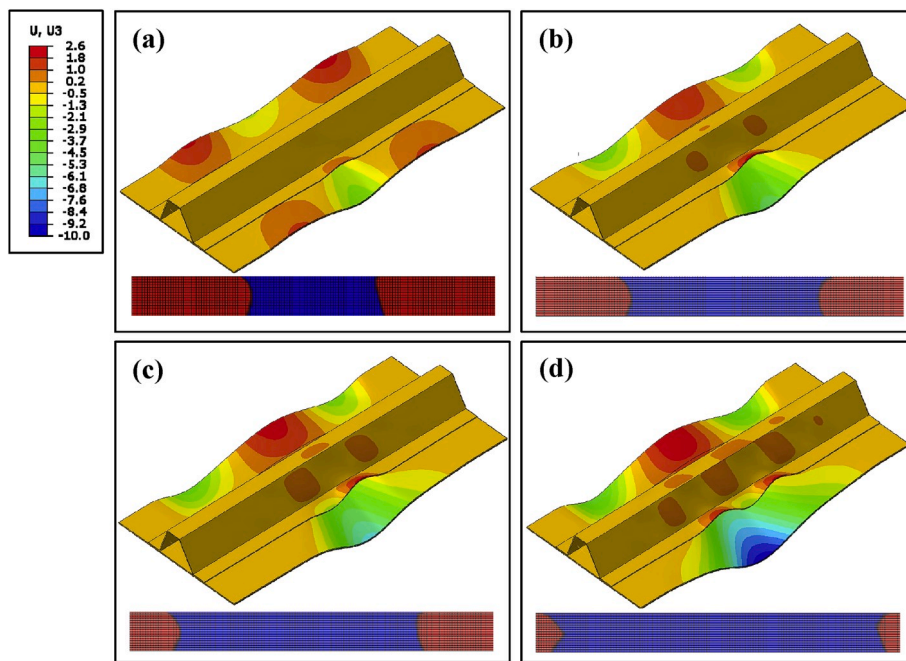
therefore the delamination growth onset. After this point, at an applied displacement of around 0.4 mm, the numerical results and experimental data start to deviate from each other. This is due to the interface properties adopted to simulate the crack propagation, which are measured

Fig. 20. Out-of-plane displacements and delamination at different values of applied displacements of SSC specimen: (a) 0.37 mm; (b) 0.49 mm; (c) 0.62 mm; (d) 0.97 mm.

grows alternatively between the two sides. A substantial rounding of the crack front can be observed at both side of the delamination, indicating a non-uniform distribution of the energy release rate along the delamination front. To verify this behavior, in Fig. 21 the energy release rate, for each opening mode, extracted from the nodes located on one side of

the delamination front, is displayed as function of the nodal position along the flange width, before each load drop.

As shown in Fig. 21a, when the first load drop occurs, the distribution of the energy release rate is fairly constant over the width of the flange except for the inside corner, where mode I contribution drops and
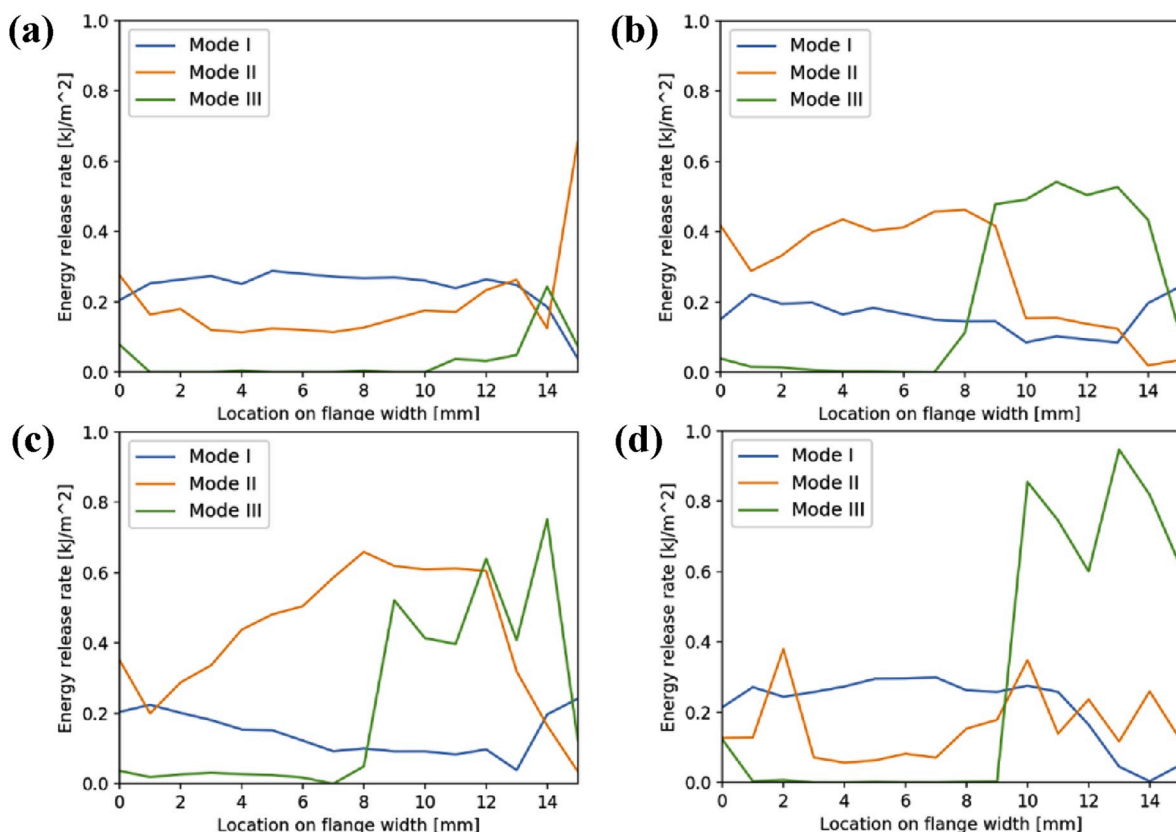

Fig. 21. Energy release rate distribution along the delamination front at: (a) 0.37 mm; (b) 0.49 mm; (c) 0.62 mm; (d) 0.97 mm.

mode II and III components increase. After this point, mode II and mode III contributions start to rise (Fig. 21b). At the third load drop, mode I is almost unchanged while the magnitude of mode II and mode III increases and the mode-mixity becomes dominated by mode III at the inside corner of the flange, as shown in Fig. 21c. At the end of the analysis mode III component increases up to 80% mode-mixity on the inner half of the stringer flange (Fig. 21d). From these consideration, it is evident that the mode-mixity is not constant along the delamination front and changes significantly as the delamination grows. Furthermore, the increase in mode III component can lead to inaccuracies in numerical analysis since in the Benzeggagh-Kenane relation (Eq. (4)), mode II and mode III are considered together and this is valid only when the mode III component is small or negligible.

In Fig. 22, the out-of-plane displacements obtained by the analysis are compared to the DIC data measured during the test just before the delamination starts to propagate [25].

As it can be noted, the numerical and experimental post-buckling shapes match very well. The skin as well as the skin portion under the stringer buckle with three half-waves, however, the direction of the numerical displacements is opposite with respect to the experimental data. In Fig. 23, the comparison in terms of out-of-plane displacements is presented after the opening of the delamination, just before the global collapse of the specimen.

The post-buckling shape obtained from the analysis perfectly agrees with that one measured with the DIC. On the delamination side of the specimen, the skin presents a large single half-wave, which extends for almost the full length of the specimen, while on the opposite side exhibits a three half-waves mode shape.

After the quasi-static investigation, the SSC specimen is analyzed under fatigue loads. The analysis is performed under load controlled condition to reproduce the experimental procedure. The two experimental tests were conducted at a maximum load of 23 kN, however, because this load is higher than the load at which the delamination starts to propagate according to the quasi-static analysis, it cannot be used for the fatigue propagation analysis because the delamination would propagate entirely after the first cycle. For this reason, a maximum load of 13.8 kN, just before the beginning of quasi-static crack propagation, is adopted. The fatigue analysis of the SSC specimen is performed using the fatigue crack growth approach adopted for the DCB and MMB specimens. A triangular load cycle is defined with maximum load equal to 13.8 kN and minimum load of 1.38 kN. Although, as shown in Fig. 21, the mode-mixity changes along the delamination front and during the propagation, the fatigue parameters are not updated during the ABAQUS analysis and, therefore the parameters for 20% mixed-mode, taken from literature [32] and reported in Table 7, are adopted for this problem. This value of the mixed-mode is chosen because it represents a

good approximation of the average mode-mixity through the whole analysis. The default value of 0.1 is adopted for the release tolerance ΔD_{Ntol}.

The analysis was performed on an Intel Xeon E5-2640 v4 using 20 cores requiring approximatively a total of 97 h of CPU time to complete.

In Fig. 24, the out-of-plane displacements of the specimen are reported at minimum and maximum load of the first cycle and at maximum load after 28836 cycles, when the fatigue analysis is terminated.

From Fig. 24, it is possible to appreciate how, during a single load cycle, the SSC specimen oscillates between pre- and post-buckling conditions. Furthermore, the increase of the out-of-plane displacements at the end of the analysis with respect to the first cycle is evident. This is due to the growth of the delamination which causes a reduction of the global stiffness of the specimen and an increase of the applied compressive displacement. At the beginning of the analysis, the flange of the stringer follows the buckling direction of the skin while, as the delamination length increases, right before the last load cycle, it starts to buckle in the opposite direction resulting in a rapidly increase of the energy release rate at the delamination front. The delamination front is shown in Fig. 25 at different load cycles compared with the experimental image taken using an ultrasound system after 24,000 cycles.

The delamination grows from an initial length of 40 mm to a length of 53.4 mm averaged over the width of the flange at the end of the simulation. It starts to propagate from the corners of the tied interface between the skin and the stringer and slowly grows up to 26329 cycles. After this point the growth rate rapidly increases due to the local buckling of the stringer flange which causes the opening of the delamination and the termination of the analysis.

The comparison with experimental results shows a quite large underestimation of the delamination length. Several causes can be identified to explain the lower growth rate of the numerical analysis. The first and most important is that the numerical compressive load is much lower than the load applied during the test. The second issue regards the coefficients of the Paris law which are defined in advance and kept constant during the analysis and therefore do not take into account possible changes in the mode-mixity or stress ratio. Finally, more experimental data of the SSC specimens are needed to validate the numerical results. Test data from only two specimens were available, and they exhibited a substantial scatter in the observed fatigue delamination growth rates.

5. Conclusions

The numerical investigation of delamination growth under quasi-static and fatigue load using an approach based on Virtual Crack
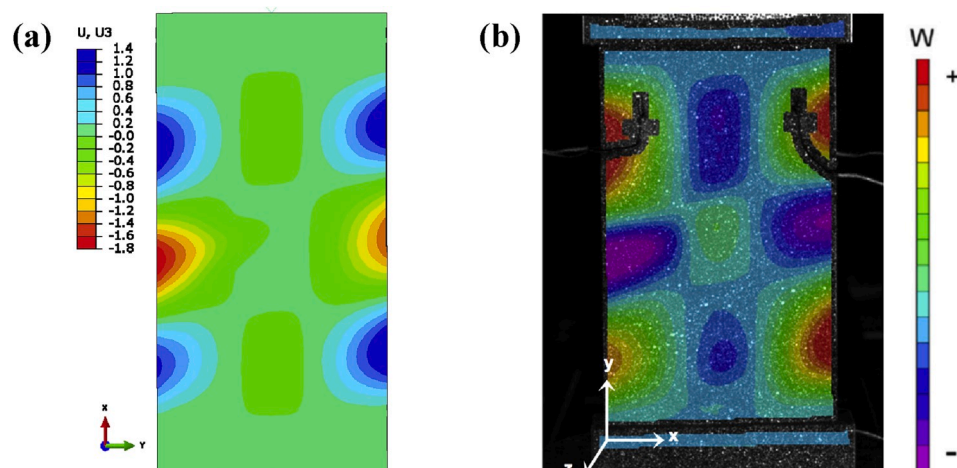

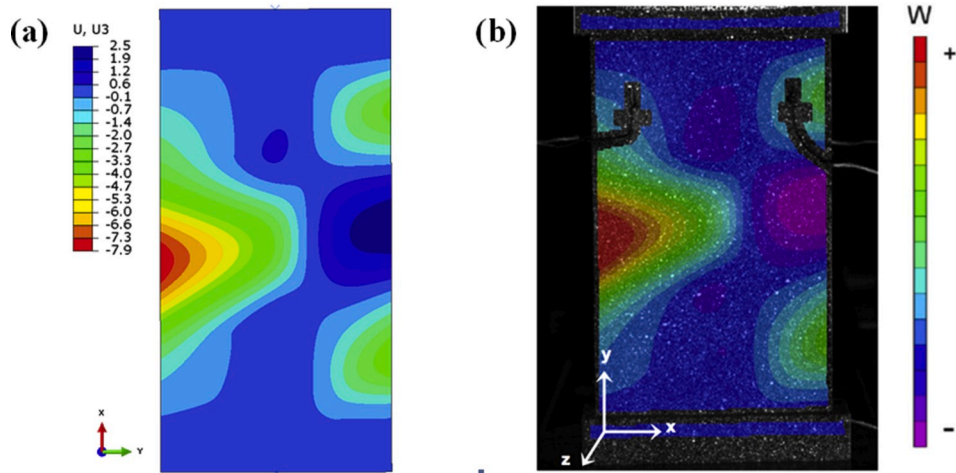**Fig. 22.** Out-of-plane displacements before delamination growth onset: (a) numerical results; (b) DIC data.

Fig. 23. Out-of-plane displacements after opening of delamination: (a) numerical results; (b) DIC data.

Table 7
Fatigue parameters of 20% mixed-mode IM7/8552.

Fatigue parameters	
R	0.1
c1	1.8E-6
c2	−11.1
c3	2412
c4	8.4
r1	0.264
r2	0.9

Closure Technique and available in the finite element code ABAQUS has been conducted. At first, Double Cantilever Beam and the Mixed Mode Bending specimens have been analyzed under quasi-static and fatigue loads to evaluate the capabilities of the numerical procedure. In both cases, the adopted methodology has produced good results in terms of crack length as function of the number of cycles compared to data taken from literature. Then, a single-stringer specimen has been analyzed under both quasi-static and fatigue loading conditions and the results have been compared with experimental data. The numerical approach has been proven to be capable of predicting delamination growth in a post-buckled single-stringer compression specimen, however, a few limitations have been encountered. During the quasi-static analysis, the lack of experimental data regarding the value of the interface properties
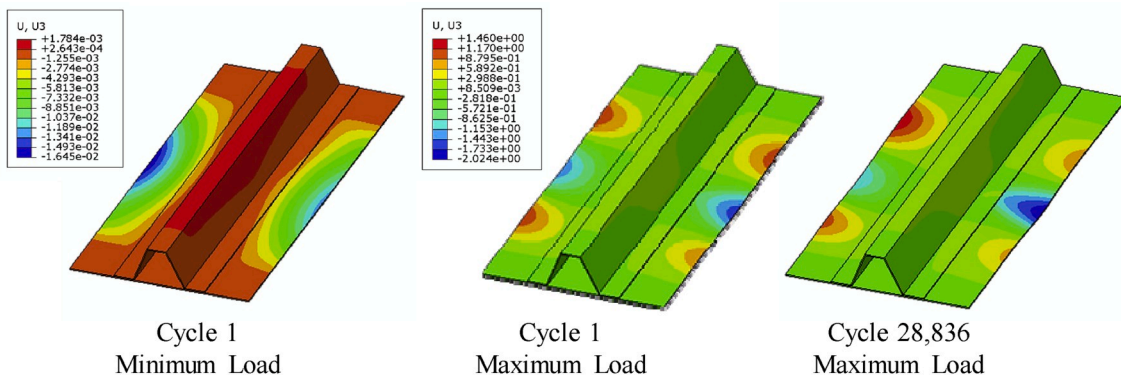

Cycle 1
Minimum Load

Cycle 1
Maximum Load

Cycle 28,836
Maximum Load

Fig. 24. Out-of-plane displacements of SSC fatigue specimen.

(a)

53.4 mm

Cycle 1

Cycle 26,329

Cycle 28,803

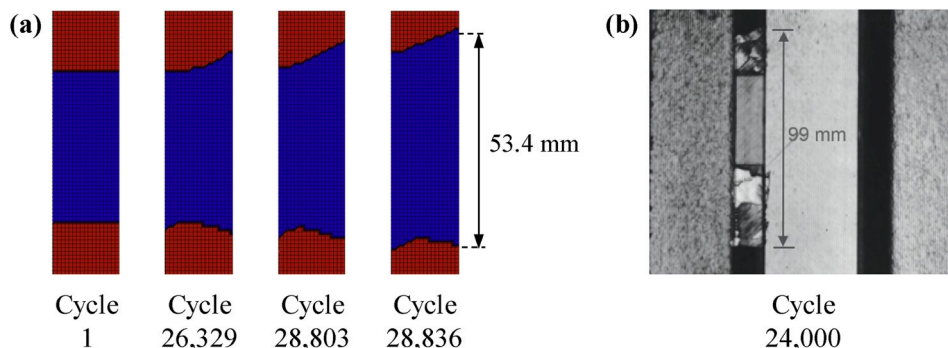Cycle 28,836

(b)

99 mm

Cycle 24,000

Fig. 25. Delamination front: (a) numerical at different load cycles; (b) experimental at cycle 24,000.

for delamination positioned between different oriented plies has led to an overestimation of the crack propagation. In the fatigue analysis, the use of a single set of Paris law parameters, related to specific values of load ratio and mode-mixity without taking into account their variation during the analysis resulted in an underestimation of the crack growth rate. Despite these limitations, the results obtained from the numerical analysis are qualitatively similar to the experimental data, showing the potential of the adopted numerical approach for the simulation of delamination growth under fatigue loading condition in complex structural problems.

Declaration of competing interests

The authors declare that they have no known competing financial interests or personal relationships that could have appeared to influence the work reported in this paper.

Acknowledgments

References

[1] Kong CW, Lee IC, Kim CG, Hong CS. Postbuckling and failure of stiffened composite panels under axial compression. Compos Struct 1998;42(1):13–21.

[2] Paris PC, Gomez MP, Anderson WE. A rational analytic theory of fatigue. Trend Eng 1961;13(9):9–14.

[3] Paris PC, Erdogan F. A critical analysis of crack propagation laws. J. Basic. Eng. 1963;85(4):528–33.

[4] Bak BLV, Sarrado C, Turon A, Costa J. Delamination under fatigue loads in composite laminates: a review on the observed phenomenology and computational methods. Appl Mech Rev 2014;66(6):1–24.

[5] Turon A, González EV, Sarrado C, Guillamet G, Maimí P. Accurate simulation of delamination under mixed-mode loading using a cohesive model with a mode-dependent penalty stiffness. Compos Struct 2018;184:506–11.

[6] Camanho PP, Dávila CG, de Moura M. Numerical simulation of mixed-mode progressive delamination in composite materials. J Compos Mater 2003;37:1415–38.

[7] Riccio A, Raimondo A, Di Caprio F, Fusco M, Sanità P. Experimental and numerical investigation on the crashworthiness of a composite fuselage sub-floor support system. Compos B Eng 2018;150:93–103.

[8] Riccio A, Linde P, Raimondo A, Buompane A, Sellitto A. On the use of selective stitching in stiffened composite panels to prevent skin-stringer debonding. Compos B Eng 2017;124:64–75.

[9] Turon A, Costa J, Camanho PP, Dávila CG. Simulation of delamination in composites under high-cycle fatigue. Compos Appl Sci Manuf 2007;38(11):2270–82.

[10] Pirondi A, Moroni F. Simulation of mixed-mode I/II fatigue crack propagation in adhesive joints with a modified cohesive zone model. J Adhes Sci Technol 2011;25 (18):2483–99.

[11] Landry B, LaPlante G. Modeling delamination growth in composites under fatigue loadings of varying amplitudes. Compos B Eng 2012;43(2):533–41.

[12] Raimondo A, Bisagni C. Analysis of local stress ratio for delamination in composites under fatigue loads. In: AIAA Journal; 2019. https://doi.org/10.2514/1.J058465.

[13] Mabson GE, Deobald LR, Dopker B, Hoyt DM, Baylor JS, Graesser DL. Fracture interface elements for static and fatigue analysis. In: Proceedings of 16th international conferences on composite materials. Kyoto; July, 2007. Code 85393.

[14] De Carvalho NV, Krueger R. Modelling fatigue damage onset and progression in composites using an element-based virtual crack closure technique combined with the floating node method. Tech. Rep. Paper 2016;1102. NASA.

[15] Di Memmo I, Bisagni C. Fatigue simulation for damage propagation in composite structures. In: Proceedings of 32nd technical conference of the American society for composites. West Lafayette; October 2017. Paper number 135472.

[16] Rybicki EF, Kanninen EF. A finite element calculation of stress intensity factors by a modified crack closure integral. Eng Fract Mech 1977;9(4):931–8.

[17] Smith SA, Raju IS. Evaluation of stress-intensity factors using general finite-element models. Fatigue Fract. Mech. 1999;29:176–200.

[18] Raimondo A, Riccio A. Inter-laminar and intra-laminar damage evolution in composite panels with skin-stringer debonding under compression. Compos B Eng 2016;94:139–51.

[19] Zou Z, Reid SR, Li S, Soden PD. General expressions for energy–release rates for delamination in composite laminates. Proc. R. Soc. A. 2019;458:645–67.

[20] Krueger R, Deobald L, Mabson GE, Engelstad S, Rao MP, Gurvich M, et al. Guidelines for VCCT-based interlaminar fatigue and progressive failure finite element analysis. Tech. Rep. NASA/TM 2017:219663. NASA; Sept. 2017.

[21] Abaqus analysis guide. Dassault Systemes; 2017.

[22] Bisagni C, Dávila CG. Single-stringer compression specimen for the assessment of damage tolerance of postbuckled structures. J Aircr 2011;48(2):495–502.

[23] Bisagni C, Brambilla P, Dávila CG. Modeling delamination in postbuckled composite structures under static and fatigue loads. In: Proceedings of international SAMPE technical conference. Long Beach; May, 2013. p. 1035–49.

[24] Bisagni C, Dávila CG. Experimental investigation of the postbuckling response and collapse of a single-stringer specimen. Compos Struct 2014;108:493–503.

[25] Dávila CG, Bisagni C. Fatigue life and damage tolerance of postbuckled composite stiffened structures with initial delamination. Compos Struct 2017;161:73–84.

[26] Dávila CG, Bisagni C. Fatigue life and damage tolerance of postbuckled composite stiffened structures with indentation damage. J Compos Mater 2018;52(7):931–43.

[27] Pascoe JA, Alderliesten RC, Benedictus R. Methods for the prediction of fatigue delamination growth in composites and adhesive bonds – a critical review. Eng Fract Mech 2013;112–113:72–96.

[28] Irwin GR. Fracture I. In: Flügge editor. Handbuch der Physik VI; 1958. p. 558–90.

[29] Benzeggagh ML, Kenane M. Measurement of mixed-mode delamination fracture toughness of unidirectional glass/epoxy composites with mixed-mode bending apparatus. Compos Sci Technol 1996;56:439–49.

[30] Krueger R. An approach to assess delamination propagation simulation capabilities in commercial finite element codes. NASA; Apr. 2008. Tech. Rep. NASA/TM-2008-215123.

[31] Krueger R. Development of a benchmark example for delamination fatigue growth prediction. NASA; July 2010. Tech. Rep. NASA/CR-2010-216723.

[32] Krueger R. Development and application of benchmark examples for mixed-mode I/II quasistatic delamination propagation predictions. NASA; Apr. 2012. Tech. Rep. NASA/CR-2012-217562.

[33] ASTM D5528-13. Standard test method for mode I interlaminar fracture toughness of unidirectional fiber-reinforced polymer matrix composites. West Conshohocken, PA: ASTM International; 2013.

[34] ASTM D6115-97(2019). Standard test method for mode I fatigue delamination growth onset of unidirectional fiber-reinforced polymer matrix composites. West Conshohocken, PA: ASTM International; 2019.

[35] ASTM D6671/D6671M-19. Standard test method for mixed mode I-mode II interlaminar fracture toughness of unidirectional fiber reinforced polymer matrix composites. West Conshohocken, PA: ASTM International; 2019.